Effects of radial electric field on kinetic ballooning mode in toroidal plasma

View Online   Export Citation   CrossMark

Y. C. Chen,[1] (iD) Y. Q. Qin,[1] (iD) G. Y. Sun,[1,a)] (iD) G. Dong,[2] (iD) Y. Xiao,[3] (iD) and Z. Lin[4] (iD)

AFFILIATIONS

[1]Department of Physics, Xiamen University, Xiamen 361000, China
[2]Princeton Plasma Physics Laboratory, Princeton University, Princeton, New Jersey 08540, USA
[3]Institute for Fusion Theory and Simulation, Department of Physics, Zhejiang University, Hangzhou 310027, China
[4]Department of Physics and Astronomy, University of California, Irvine, California 92697, USA

[a)]Author to whom correspondence should be addressed: gysun@xmu.edu.cn

ABSTRACT

Global gyrokinetic particle simulations show that the radial electric field (E_r) shear can suppress the kinetic ballooning mode (KBM) in a toroidal plasma. The linear KBM growth rate reaches a maximum when the toroidal rotation induced by the ion diamagnetic shear is canceled by the $E \times B$ flow shear. High toroidal-mode-number (high-n) KBMs are more sensitive to the E_r shear than low-n KBMs. Nonlinear simulations find that both the E_r shear and a self-generated zonal flow can reduce the nonlinear KBM saturation level with smaller particle and ion heat transport. Meanwhile, the zonal flow can weaken the suppressing effects of the E_r shear on KBM nonlinear saturation amplitude. The radial correlation length of the turbulence is reduced by the E_r shear and the zonal flow.

Published under an exclusive license by AIP Publishing. https://doi.org/10.1063/5.0131294

I. INTRODUCTION

The high confinement mode (H-mode) found in the ASDEX Tokamak is still considered the operation mode for the International Thermonuclear Experimental Reactor (ITER) to get a better fusion discharge performance of deuterium–tritium (D–T) plasma.[1,2] However, the edge localized modes (ELMs) that typically exist in the pedestal region under H-mode operation severely erode the plasma-facing components (mainly the divertor) because of periodic and transient energy flow.[3] The kinetic ballooning mode (KBM) is driven by an enormous pedestal pressure gradient and is a crucial electromagnetic microinstability that affects the physical properties in the pedestal region.[4,5] The Environmental Processes and Effects Division (EPED) model has been used to show that the KBM during ELM cycles has a regulating effect on the pedestal pressure gradient by constraining the pedestal width.[6] Although there is a strong peak in the bootstrap current in the pedestal region, the KBM can couple with peeling balloon-ing modes (PBMs) to limit the maximum pedestal height.[7] Although the linear properties of KBMs are well understood, a complete understanding of the properties of nonlinear KBMs remains elusive.

The dependence of the KBM on the parallel-ion compressibility, the width of the radial equilibrium profile, and resonant magnetic perturbations (RMPs) has been previously investigated.[8–10] The parallel-ion conductivity can decrease the KBM growth rate under a positive magnetic shear and has no effect on the KBM under a negative magnetic shear.[8] It has been demonstrated that the KBM growth rate and frequency are very sensitive to the radial width of the equilibrium density and temperature profile.[9,11] Kinetic simulations reveal that in the presence of a plasma kink, resonant magnetic perturbations (RMPs) have no significant effect on the KBM growth rate.[10] In addition, it is widely accepted that the radial electric field (E_r) plays an important role in cross field transport and L–H mode transition in the edge region,[12] which suggests that E_r may affect the KBM instability. The radial electric field can be deduced theoretically from the radial force balance equation[13] and experimentally measured by active charge exchange recombination spectroscopy[14] (CXRS) or the motional stark effect[15] (MSE) experimentally. It has been found that the radial electric field can balance the thermal-ion orbit loss current by providing a return current.[16] The width of the established edge E_r well can be considered as the H-mode pedestal width.[17] Furthermore, a sheared radial electric field can lead to a sheared plasma flow via a mechanism of the $E \times B$ velocity shearing. This sheared flow effectively breaks up turbulence eddies and reduces the radial correlation length of the turbulence, leading to suppression of the turbulent

transport at the plasma edge.[18] The shear straining can lower correlation lengths in the direction of shear and reduces turbulent amplitudes.[19] It has been proven that the E_r-induced poloidal rotation can significantly reduce the growth rate of the ion temperature gradient (ITG).[20] In magnetohydrodynamics (MHD) simulations of linear PBM using BOUT++, E_r has been found to have destabilizing effects for low n and stabilizing effects for high n.[21] Using the GEM code and considering the diamagnetic drift and finite Larmor radius effects has shown that the E_r shear can decrease the particle flux for the kinetic peeling ballooning mode (KPBM) during both the linear and nonlinear stages.[22] In this paper, we investigate the effects of E_r and its shear on the KBM using the gyrokinetic toroidal code (GTC), which incorporates diamagnetic drift and finite Larmor radius effects. Furthermore, both a perturbed parallel magnetic field and an equilibrium current are considered because both of them can destabilize the KBM. In addition, the performance comparison of the E_r shear on KBM in the cases with and without zonal flow is obtained in this study.

GTC is a well benchmarked full torus particle-in-cell (PIC) code derived from first principles for simulating multiple physics processes, including microturbulence, energetic particle physics, and kinetic modes in fusion plasmas. An expansion of the electron response using the electron–ion mass ratio as a small parameter has been used to develop a fluid-kinetic hybrid electron model that overcomes numerical difficulties, such as the parallel Courant condition, high-frequency ω_H, and tearing mode, for both electrostatic and electromagnetic simulations.[23,24] A conservative scheme of kinetic electrons was subsequently developed for minimizing the electron particle noise and preventing cancellation from the parallel electric field due to calculating the nonadiabatic vector potential using Ohm's law.[25] Both hybrid and conservative models are used in GTC to implement the electromagnetic capability in KBM simulations.[24,26]

GTC has been used to perform electrostatic simulations to identify the effects of E_r and its shear on ITG in toroidal plasma and field-reversed configurations. Linear simulations have shown that the $E \times B$ flow shear reduces the KBM growth rate and distorts turbulent eddies in the toroidal plane.[27,28] Nonlinear simulations have shown that the E_r shear can decrease the ITG saturation amplitude and particle flux.[27–29]

In this study, a linear electromagnetic simulation is performed on the KBM with cyclone base case parameters[9] using fluid, hybrid and conservative electron models. Identical results for the linear growth rate and real frequency are obtained from simulations using the hybrid and conservative models, where the KBM growth rate obtained using both models is lower than that obtained using the fluid model due to the effects of kinetic electrons. Consistency of the Doppler frequency shift between simulation and theory has been shown for rigid rotation in a plasma with a constant E_r profile. Linear simulations show that the E_r flow shear has a stabilizing effect on the KBM, where this effect becomes stronger with increasing E_r shear. In addition, the E_r shear effects are more significant for high-n KBMs than low-n KBMs due to a larger effective shearing rate. Nonlinear simulations show that the E_r shear reduces the saturation level amplitude, the particle diffusivity and ion heat conductivity, which is similar to the turbulence suppression by the self-generated zonal flow. The effects of E_r shear on KBM nonlinear saturation amplitude are weakened by the zonal flow. It is found that the E_r shear can suppress the spread of KBM turbulence from the linear phase to the nonlinear phase and reduce the radial correlation length of the turbulence.

The remainder of this paper is organized as follows. The GTC simulation models for the KBM are described in Sec. II. In Sec. III, the results of simulations showing the effects of E_r on the linear KBM instability are presented. The effects of E_r shear on KBM nonlinear saturation amplitude are discussed in Sec. IV. A brief summary of the study is presented in Sec. V.

II. SIMULATION SETUP

In our simulations, collisionless gyrokinetic Vlasov equation in the five-dimensional phase space[30] is used for describing ions

$$\frac{d}{dt}f(\boldsymbol{X}, \mu, v_{\parallel}, t) = \left(\frac{\partial}{\partial t} + \dot{\boldsymbol{X}} \cdot \nabla + \dot{v}_{\parallel}\frac{\partial}{\partial v_{\parallel}}\right)f = 0, \quad (1)$$

where

$$\dot{\boldsymbol{X}} = v_{\parallel}\frac{\boldsymbol{B}}{B_0} + \boldsymbol{v}_{\delta E} + \boldsymbol{v}_d + \boldsymbol{v}_{B_{\parallel}} + \boldsymbol{v}_{zf} + \boldsymbol{v}_{er}, \quad (2)$$

$$\dot{v}_{\parallel} = -\frac{1}{m}\left(\frac{\boldsymbol{B}^*}{B_0} \cdot (\mu\nabla B_0 + Z\nabla(\phi + \mu\delta B_{\parallel})) + \frac{Z}{c}\frac{\partial A_{\parallel}}{\partial t}\right). \quad (3)$$

$\boldsymbol{X}$, μ, and $v_{\parallel}$ denote the gyrocenter position, magnetic moment, and parallel velocity, respectively. Defining $\boldsymbol{b}_0 \equiv \frac{\boldsymbol{B}_0}{B_0}$, $\boldsymbol{B}^* = \boldsymbol{B} + \frac{B_0 v_{\parallel}}{\Omega}\nabla \times \boldsymbol{b}_0$ (Ω is the cyclone frequency) is the modified magnetic field for motion equation, $\boldsymbol{B} = \boldsymbol{B}_0 + \nabla \times (A_{\parallel}\boldsymbol{b}_0)$ the magnetic field, $\boldsymbol{v}_{\delta E} = \frac{c\boldsymbol{b}_0 \times \nabla\delta\phi}{B_0}$ the drift velocity of perturbed electric field, $\boldsymbol{v}_d = \frac{c}{ZB_0}(mv_{\parallel}^2\nabla \times \boldsymbol{b}_0 + \mu\boldsymbol{b}_0 \times \nabla B_0)$ the equilibrium magnetic drift velocity, $\boldsymbol{v}_{B_{\parallel}} = \boldsymbol{b}_0 \cdot \nabla \times \delta\boldsymbol{A}_{\perp}$ the drift for perturbed parallel magnetic field,[31] $\boldsymbol{v}_{zf} = \frac{c\boldsymbol{b}_0 \times \nabla\phi_{zf}}{B_0}$ the zonal flow velocity, $\boldsymbol{v}_{er} = \frac{c\boldsymbol{b}_0 \times \nabla\phi_{er}}{B_0}$ the drift velocity of equilibrium radial electric field, $\phi = \delta\phi + \phi_{zf} + \phi_{er}$ (ϕ_{zf} and ϕ_{er} are the electrostatic potential of the zonal flow and equilibrium radial electric field, respectively) the electrostatic potential. In addition, the electrostatic potential is calculated by gyrokinetic Poisson's equation while gyrokinetic parallel and perpendicular Ampère's law are used for obtaining the parallel and perpendicular magnetic vector potential, respectively. A perturbative (δf) method[32] has been developed in GTC for reducing particle noise of full-f method. In δf method, the distribution function is separated to equilibrium and perturbed parts, i.e., $f = f_0 + \delta f$. Defining the propagator $\frac{d}{dt} \equiv L = L_0 + L_{zf} + \delta L$, then Eq. (1) can be written as $Lf = (L_0 + L_{zf} + \delta L)(f_0 + \delta f) = 0$, where

$$L_0 = \frac{\partial}{\partial t} + \left(v_{\parallel}\frac{\boldsymbol{B}}{B_0} + \boldsymbol{v}_d + \boldsymbol{v}_{er}\right) \cdot \nabla$$
$$- \frac{1}{m}\left(\frac{\boldsymbol{B}^*}{B_0} \cdot (\mu\nabla B_0 + Z\nabla\phi_{er})\right)\frac{\partial}{m\partial v_{\parallel}}, \quad (4)$$

$$L_{zf} = \boldsymbol{v}_{zf} \cdot \nabla - \frac{Z}{mB_0}(\boldsymbol{B}^* \cdot \nabla\phi_{zf})\frac{\partial}{\partial v_{\parallel}}, \quad (5)$$

$$\delta L = \left(v_{\parallel}\frac{\nabla \times A_{\parallel}\boldsymbol{b}_0}{B_0} + \boldsymbol{v}_{\delta E} + \boldsymbol{v}_{B_{\parallel}}\right) \cdot \nabla$$
$$- \frac{1}{m}\left(\frac{\nabla \times A_{\parallel}\boldsymbol{b}_0}{B_0} \cdot \mu\nabla B_0 - \frac{\boldsymbol{B}^*}{B_0}Z\nabla(\delta\phi + \mu\delta B_{\parallel})\right)\frac{\partial}{\partial v_{\parallel}}$$
$$- \frac{\partial A_{\parallel}}{\partial t}\frac{Z\partial}{m\partial v_{\parallel}}. \quad (6)$$

The equilibrium part f_0 is defined as $L_0 f_0 = 0$ and could be approximated as a shifted Maxwellian's distributions as follows:

$f_0 = n_0 (\frac{m}{2\pi T})^{\frac{3}{2}} \exp\left(-\frac{m(v_{\parallel}-v_{\parallel 0})^2+2\mu B_0}{2T}\right)$, where $v_{\parallel 0}$ is the equilibrium parallel velocity. For calculating perturbed part δf, we define the particle weight as $w \equiv \frac{\delta f}{f}$. Then, we can obtain

$$\frac{d}{dt}w = -(1-w)\left[\left(v_{\parallel}\frac{\nabla \times A_{\parallel}\boldsymbol{b_0}}{B_0} + \boldsymbol{v_{zf}}\right) \cdot \frac{\nabla f_0}{f_0}\right.$$
$$-\frac{1}{mf_0}\left(\frac{\nabla \times (A_{\parallel}\boldsymbol{b_0})}{B_0} \cdot \mu\nabla B_0 - \frac{\boldsymbol{B^*}}{B_0}Z\nabla(\delta\phi + \phi_{zf} + \mu\delta B_{\parallel})\right)$$
$$\left.\times \frac{\partial f_0}{\partial v_{\parallel}} - \frac{\partial A_{\parallel}}{\partial t}\frac{Z\partial f_0}{mf_0\partial v_{\parallel}}\right]. \tag{7}$$

Instead of drift-kinetic equation for all electrons, the fluid-kinetic hybrid electron model mentioned above takes electrons response apart into adiabatic part in the lowest order and nonadiabatic part in the higher order. That is, the distribution function for electrons f_e can be simply expressed as $f_e = f_0 e^{e\Phi/T_e} + \delta g_e^{(1)} + \delta g_e^{(2)} + \cdots$, where Φ is the parallel electric field potential, and the first term is the lowest order for describing adiabatic electrons and calculated by fluid equation, which removes numerical difficulties associated with the tearing modes and the electron Courant condition. The higher order nonadiabatic response $\delta g_e^{(\cdot)}$ is treated kinetically with all the nonlinear kinetic effects preserved. Based on hybrid model, the electromagnetic conservative scheme for electrons further separates the parallel vector potential into adiabatic part and nonadiabatic part that can be solved by analytic solution and Ohm's law, respectively. Note that the adiabatic electrons have a simple relation between perturbed electron density and perturbed potential: $\frac{\delta n_e}{n_0} = -e\frac{\delta\phi}{T}$. In the limit of long wavelength and no parallel electric field, our equations reduce to the well-known ideal MHD equations. More details for electron models are described in Refs. 24 and 25.

The cyclone base case parameters employed for background plasma are as follows: the inverse aspect ratio $a/R_0 = 0.357$, where $R_0 = 83.5$ cm and a are the major radius and the minor radius, respectively. The ion gyro-radius is $\rho_i = 2.86 \times 10^{-3}R_0$. The radial profile of safety factor is $q = 0.82 + 1.1\psi_N + 1.0\psi_N^2$ in which $\psi_N = \psi/\psi_w$ (ψ is the poloidal magnetic flux and $\psi_w = 0.0375B_0R_0^2$ the magnetic flux at the wall) is the poloidal magnetic flux normalized to the separatrix value. The equilibrium radial profile of density and temperature is given by $a_0(1 + a_1(\tanh((a_2 - \psi_N)/a_3) - 1))$. The parameter a_0 in density is 1.2×10^{13} cm^{-3} and 5.8 keV in temperature. In addition, parameters of (a_1, a_2, a_3) are $(0.205, 0.3, 0.4)$ and $(0.415, 0.18, 0.4)$ for density and temperature, respectively. The radial profile of equilibrium density n, temperature T, and safety factor q are shown in Fig. 1. The simulation parameters at the diagnostic flux surface of $\psi_N = 0.389$ are $q = 1.4$, $B_0 = 2$ T, $T_e = T_i = 2223$ eV, $n_e = n_i = 9 \times 10^{13}$ cm^{-3}, $R_0/L_T = 6.9$, $R_0/L_n = 2.2$, $=0.78$, $\beta_e = 2.0\%$, where $L_T^{-1} = -d \ln T/dr$ is the scale lengths of temperature, $L_n^{-1} = -d \ln n/dr$ the scale lengths of density, $s = d \ln q/dr$ the magnetic shear, and $\beta_e = 8\pi n T_e/B_0^2$, respectively. In our simulation case with $n = 10$, the radial, poloidal, and toroidal grid numbers are 100, 400, and 32, respectively, based on the convergence test. The number of particle cell is 50 for thermal ions and electrons, and the poloidal grid numbers should
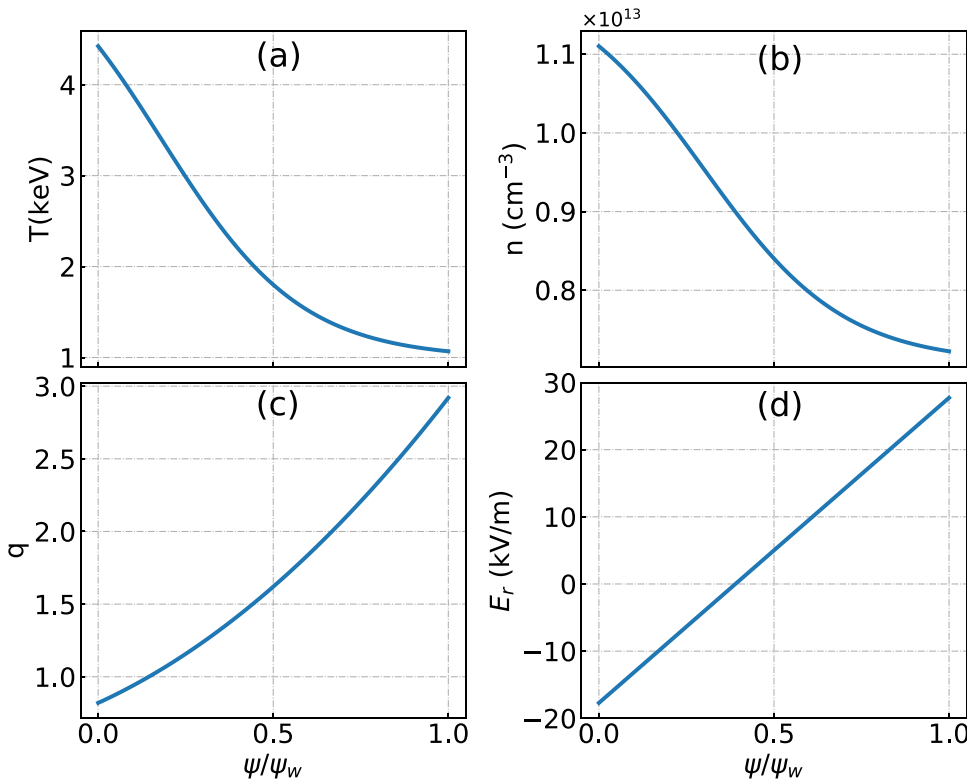

FIG. 1. Radial profile of equilibrium temperature T [panel (a)], equilibrium density n [panel (b)], safety factor q [panel (c)], and radial electric field E_r with a constant shear $\omega_s = 0.4C_s/R_0$ [panel (d)].
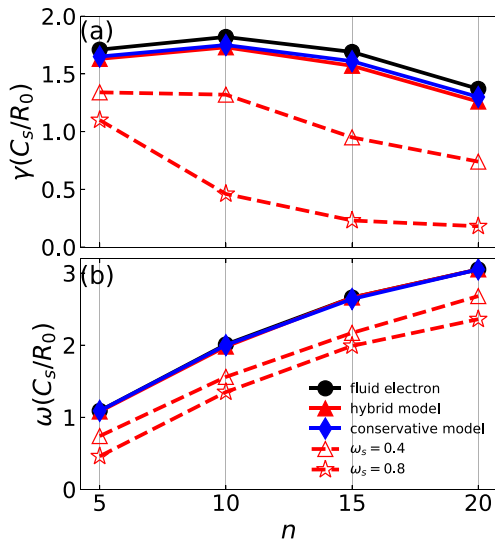
FIG. 2. Growth rate γ [panel (a)] and real frequency ω [panel (b)] of KBM in linear simulations as a function of toroidal mode numbers n. Solid lines are the cases carried out by fluid electron, hybrid and conservative models, with the absence of E_r. Both hybrid and conservative models are with kinetic electrons. Dashed lines show the cases with E_r shear $\omega_s = 0.4 C_s/R_0$ (triangle) and $\omega_s = 0.8 C_s/R_0$ (star) in hybrid model.

be set larger as n increases. The time step size is $\Delta t = 0.002 R_0/C_s$, where $C_s = \sqrt{T_e/m_i}$ is the ion sounds speed.

III. EFFECTS OF RADIAL ELECTRIC FIELD ON LINEAR KBM INSTABILITY

With the cyclone base case parameters and without adding equilibrium radial electric field (i.e., $\phi_{er} = 0$), Figs. 2(a) and 2(b) show that the growth rate γ and real frequency ω of linear KBM simulations, respectively, with different toroidal mode number n. Here, the corresponding poloidal mode numbers m of the largest growth rate satisfy $q = m/n$ on diagnostic surface. Thus, the mode of highest amplitude is chosen to get the largest the growth rate. Figure 2(a) shows that the KBM growth rate becomes large with the increasing of n and reach peak at $n = 10$ among the three electron models, indicating that dominant instability of KBM at diagnostic surface is around $n = 10$ in this case. Compared with fluid electron model, the KBM growth rate is around $0.1 C_s/R_0$ decrease in hybrid and conservative models due to the effects of finite Larmor radius and trapped electrons of kinetic electrons.[33,34] The almost same results of KBM real frequency are obtained for different electrons models, as shown in Fig. 2(b), the physical reason lies in that ω is mainly dependent on ion dynamics.[26] Note that the simulation results are similar between hybrid model and conservative model, and we will use hybrid model for the cases with kinetic electrons in Secs. III and IV.

It has already been proven using various gyrokinetic simulation codes that a radial electric field can significantly affect the properties of edge turbulence in the pedestal region.[22,35–39] In our simulation, the radial electric field is given by $E_r = -\frac{\partial \phi_{er}}{\partial \psi}|\nabla \psi|$, and a constant E_r, i.e., there is no rotational E_r shear across the entire plasma, is first added to verify the rigid rotation effects of E_r. We have verified a Doppler

frequency shift for M ranging from 0 to 0.3, where $M = v_{\parallel 0}/C_s$ is the Mach number with $v_{\parallel 0} \approx R\Omega_\phi$. The equilibrium angular frequency of the toroidal rotation Ω_ϕ is calculated from the radial force balance $\Omega_\phi \approx -\Omega_{er} + q\Omega_p - \Omega_{dia}$, where Ω_p is the poloidal rotation, and $\Omega_{er} = \frac{\partial \phi_{er}}{\partial \psi}$ and $\Omega_{dia} = \frac{1}{n_i Z_i}\frac{\partial P_i}{\partial \psi}$ are the toroidal angular frequency driven by the $E \times B$ flow and the ion diamagnetic flow, respectively. Note that the poloidal component of the plasma flows of the neoclassical damping cancels the $E \times B$ flow in the poloidal direction. As expected, we see a Doppler frequency shift $\Omega_{dopp} = n\Omega_{er}$ occurs as the Mach number changes. We also find that the KBM growth rate changes by less than 2% in the absence of kinetic electrons and 5% in the presence of kinetic electrons. The effects of the rigid rotation on the KBM growth rate are small because the $E \times B$ flow speed at $M \ll 1$ is considerably smaller than the ion thermal speed. Similar results have been observed for the ITG mode in toroidal plasma and field-reversed configurations.[27,28]

The E_r shear is calculated from a two-point nonlinear analysis: $\omega_s = \frac{\Delta\psi}{\Delta\zeta}\frac{\partial\Omega_{er}}{\partial\psi} \approx \frac{(B_p R_0)^2}{B_0}\frac{\partial^2\phi_{er}}{\partial\psi^2}$,[27,40] where $\Delta\psi$ and $\Delta\zeta$ are the turbulence correlation lengths in radial and toroidal direction, respectively, and B_p is the poloidal magnetic field. For an isotropic turbulence eddy ($\Delta R \sim R\Delta\zeta$) near equatorial plane, then the shearing rate can be simplified to the radial variation of the toroidal rotation frequency: $\omega_s = \frac{\partial\Omega_{er}}{\partial\ln R}$.[28] In our simulation, the radial profile of ϕ_{er} with a constant ω_s is taken to be $\phi_{er} = \frac{\omega_s}{2B_0 R_0^2}(\psi - 0.02\psi_w)(0.88\psi_w - \psi)$, where $E_r = 0$ at the core of the simulation domain to minimize the Doppler frequency shift. The red dashed line in Fig. 1 corresponds to the radial profile of E_r with $\omega_s = 0.4 C_s/R_0$. Figure 3 shows the result of the KBM growth rate as a function of the E_r shear over the range of $-0.5 C_s/R_0$ to $0.5 C_s/R_0$, with $n = 10$ and $\beta = 2.0\%$. We can see that the KBM growth rate decreases as ω_s increases, indicating that the E_r shear has a stabilizing effect on the KBM. Note that the γ value satisfies $\gamma_{(\omega_s - 0.1 C_s/R_0)} \approx \gamma_{(-\omega_s)}$, which implies that the maximum growth rate of KBM appears approximately at the E_r shear $\omega_s = -0.05 C_s/R_0$ in this case. In our simulations, the ion diamagnetic flow shear $\omega_{dia} = \frac{\partial\Omega_{dia}}{\partial\ln R}$ equals to $0.48 C_s/R_0$, that is, $\omega_{dia} + n\omega_s \approx 0$. Therefore, we find that the maximum growth rate occurs at a radial shear of the Doppler shifted local mode frequency of zero, i.e., $\frac{\partial}{\partial\ln R}(\Omega_{dia} + \Omega_{dopp}) \approx 0$, which agrees very well with the results presented in Refs. 28 and 41.
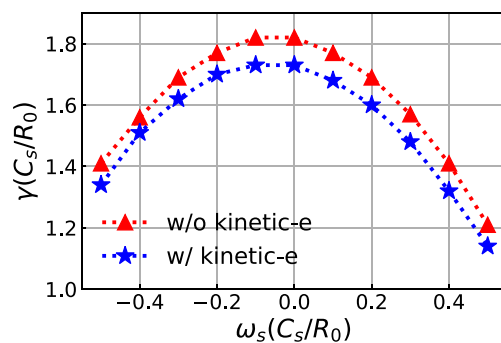

FIG. 3. Growth rate of KBM as a function of the E_r shear with (blue star) and without (red triangle) kinetic electrons in KBM linear simulation for $n = 10$ and $\beta = 2.0\%$.
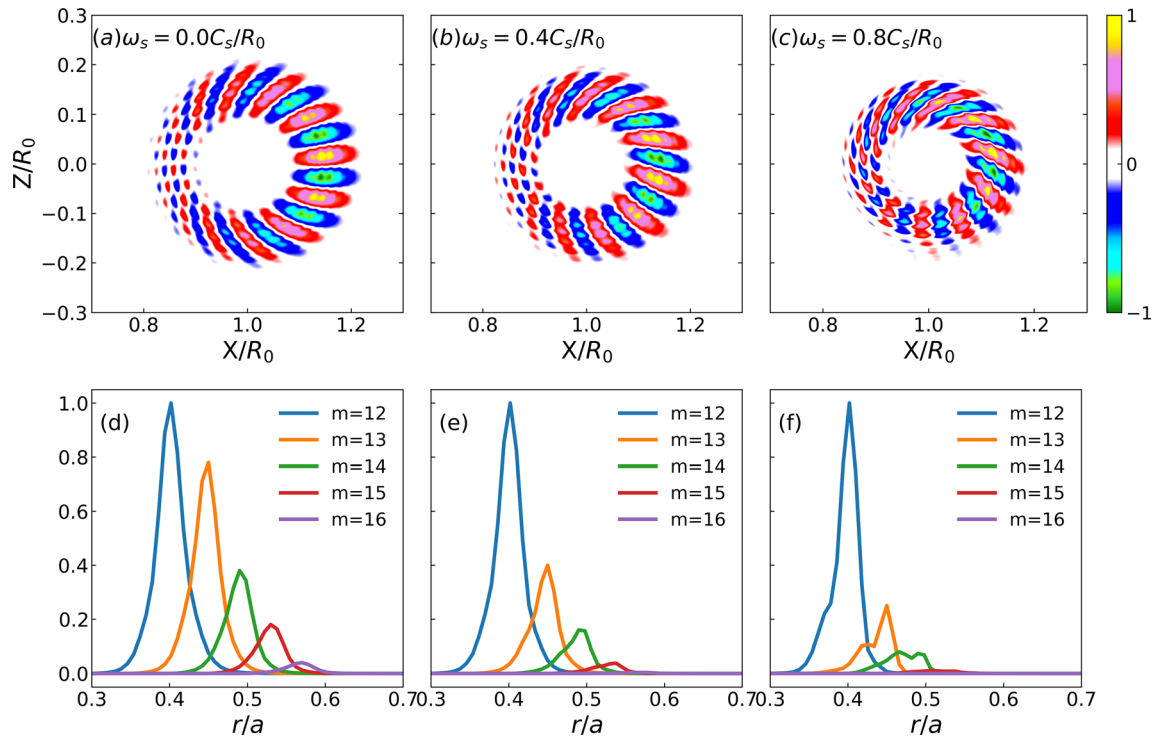
FIG. 4. Upper panels of (a)–(c) show two-dimensional poloidal contour of perturbed electrostatic potential $\delta\phi$ with $\omega_s = 0.0$, $0.4C_s/R_0$, and $0.8C_s/R_0$ in KBM linear simulation of $n = 10$ with kinetic electrons. Lower panels of (d)–(f) correspond to the radial mode profile of different poloidal mode numbers m of (a)–(c), respectively. All results here base on a same physical time of $t = 4.0R_0/C_s$.

The evolution of the poloidal contour of the perturbation electrostatic potential $\delta\phi$ at $n = 10$ and $t = 4.0R_0/C_s$ is shown in Figs. 4(a)–4(c), and the corresponding radial mode profiles of different poloidal mode numbers are shown in Figs. 4(d)–4(f). Figure 4(a) shows a ballooning structure of $\delta\phi$ with a small radial tilting due to a weak background flow at $\omega_s = 0$. Figures 4(b) and 4(c) show an E_r-induced flow that gradually becomes stronger, leading to a reduction in the radial widths of $\delta\phi$ and deformation of the ballooning structure, which implies that E_r flow shear is accompanied by effective suppression of radial plasma turbulent transport. In addition, the mode tilts in the radial direction as ω_s increases due to a radial variation in the local wave phase velocity caused by the $E \times B$ shear flow. Figure 4(d) shows that the single poloidal mode number of the $\delta\phi$ maintains a Gaussian profile at $\omega_s = 0$ and decreases from $m = 12$ to $m = 16$. As the E_r shear increases, all the harmonic modes decrease, and the Gaussian profile is lost. Figures 4(e) and 4(f) show that the highest m mode at the outer side goes to zero first, corresponding to the reduction of the radial width of $\delta\phi$ from the outer boundary shown in Figs. 4(b) and 4(c), respectively.

Figure 2 shows the stabilizing effects of E_r shear on the KBM in the linear simulations with kinetic electrons are also observed for different toroidal mode numbers n. In Fig. 2(a), the KBM growth rate decreases with increasing E_r shear, as expected. Furthermore, the suppression effect of E_r shear is stronger at higher n, such that the most unstable mode changing from $n = 10$ to 5 as ω_s increases to $0.4C_s/R_0$ or $0.8C_s/R_0$. This result is obtained because the ratio of the correlation

lengths of the ambient turbulence in the radial and toroidal directions increases with the increasing of the toroidal mode numbers, leading to an increase in the effective $E \times B$ shearing rate.[40] Figure 2(b) shows that the real frequency also decreases as ω_s increases, but the changes in ω are considerably smaller than that in γ because $E_r = 0$ is located on the diagnostic surface to minimize the Doppler frequency shift.

IV. EFFECTS OF RADIAL ELECTRIC FIELD ON KBM NONLINEAR SATURATION AMPLITUDE

It is well known that microturbulence is regulated by the spontaneous generation of the zonal flow, which may be excited by all types of microinstabilities.[29,42–44] The nonlinear physical effects for turbulence and transport have been studied in various gyrokinetic simulations.[45–50] We have demonstrated the stabilizing effect of E_r and its shear on the KBM instability in linear simulations. In this section, a comparative analysis is performed of the results of KBM nonlinear simulations in the presence of the zonal flow and sheared E_r for $n = 10$ and $\beta = 2.0\%$. The same setup is used for the nonlinear simulations as for the linear simulations. Nonlinear terms are added to the guiding center equation of motion,[51] and the zonal component is also considered in nonlinear simulation. We can ignore the zonal flow effects by artificially suppressing the zonal potential term (ϕ_{zf}) in simulations. In addition, only the hybrid electron model is used to accurately maintain the kinetic effects of the particles.

Figure 5 shows the time history of the perturbation electrostatic potential $\delta\phi$ for the mode of $n = 10$ and $m = 14$ on the diagnostic
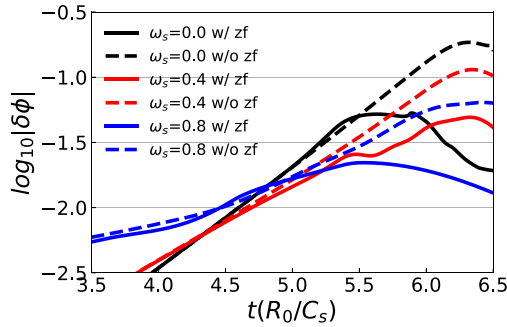
FIG. 5. The time history of the perturbed electrostatic potential $\delta\phi$ for the mode of $n = 10$, $m = 14$ on the diagnostic rational surface with (solid lines) and without (dashed lines) zonal flow as E_r shear is $\omega_s = 0.0$, $0.4C_s/R_0$, and $0.8C_s/R_0$.

rational surface. With increasing time, the amplitude of $\delta\phi$ first increases exponentially during the linear stage and then saturates during the nonlinear stage. Comparing the results of the nonlinear simulation with and without zonal flow presented in the plot shows that the zonal flow significantly reduces the amplitude of $\delta\phi$ during the nonlinear stage. By contrast, the E_r shear reduces the amplitude of

nonlinear fluctuations as well as the linear growth. Note that the saturated level is almost unchanged when $\omega_s = 0.4C_s/R_0$ with the presence of the zonal flow, which means the zonal flow is much more dominant mechanism for reducing the saturated amplitude with small E_r shear. However, we should point out that physics model in these simulations is not complete (e.g., only a single-toroidal-mode-number eigenmode family and short saturated time). We will perform more realistic nonlinear simulations and steady saturated level evolution in the future to investigate the E_r effects on microturbulence and transport.

Figure 6 shows the two-dimensional $\delta\phi$ poloidal structure in the nonlinear regime. Figure 6(a) shows the results obtained in the absence of both the zonal flow and E_r shear, where the poloidal mode structure in this panel is deformed slightly from the linear phase to the nonlinear phase [compared to the results shown in Fig. 4(a)] due to the nonlinearity of the flow. Meanwhile, the radial widths of the $\delta\phi$ turbulence are broadened because of the turbulence spreading. Figure 6(d) shows that the zonal flow reduces the $\delta\phi$ intensity and breaks up the radially elongated eigenmode structure into microscale and mesoscale structures. Figures 6(b) and 6(c) show the results of the simulation with only E_r shear for $\omega_s = 0.4C_s/R_0$ and $0.8C_s/R_0$ (without zonal flow), where the radial width of the turbulence is also
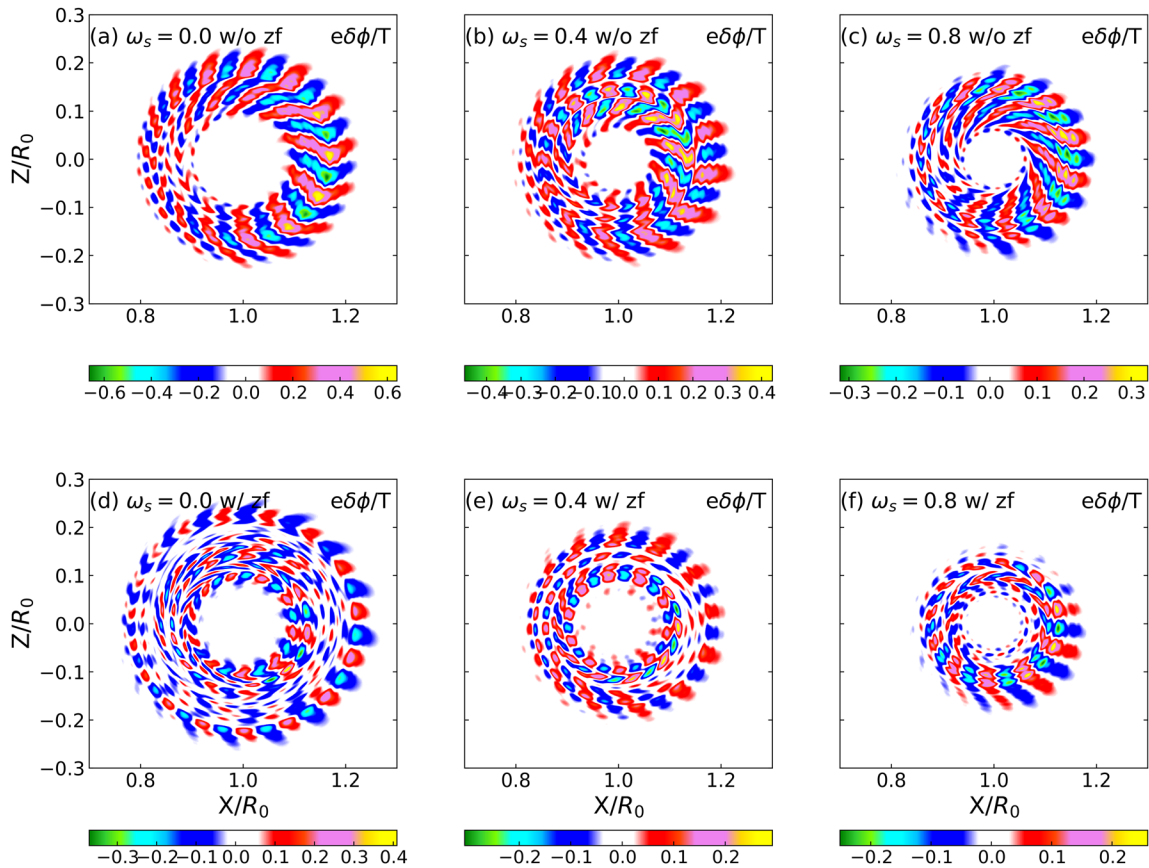

FIG. 6. Two-dimensional poloidal contour of perturbed electrostatic potential $\delta\phi$ at nonlinear saturation time $t = 6.5R_0/C_s$ with different E_r shear: (a) and (d), $\omega_s = 0$. (b) and (e), $\omega_s = 0.4C_s/R_0$. (c) and (f), $\omega_s = 0.8C_s/R_0$. Upper panels (a)–(c) are the cases without zonal flow and lower panels (d)–(f) with zonal flow.
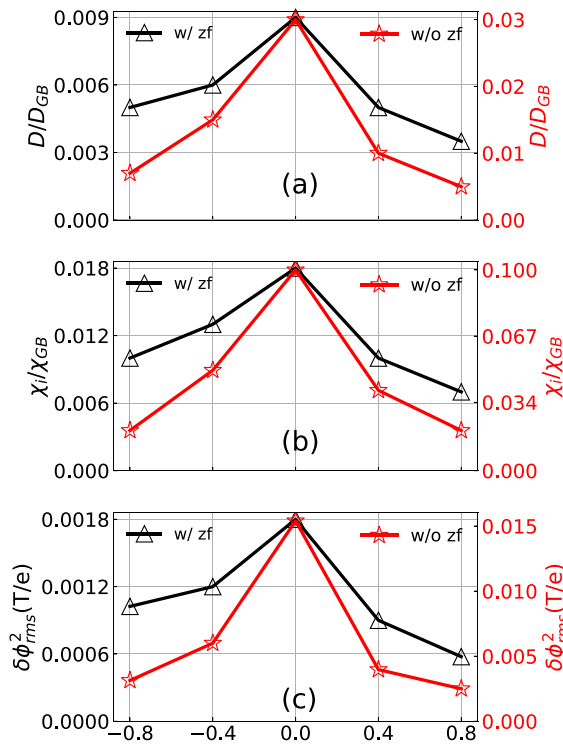
FIG. 7. The volume-averaged particle diffusivity D [panel (a)], ion heat conductivity χ_i [panel (b)], and turbulence amplitude $\delta\phi_{rms}^2$ [panel (c)] for $n = 10$ with (black triangle) and without (red star) zonal flow as a function of the E_r shear. All quantities are time-averaged over the nonlinear saturation stage during $t = [6.3, 6.5]R_0/C_s$. The quantities in the cases with zonal flow are corresponding to the left y-axis, and the right y-axis is used for the cases without zonal flow.
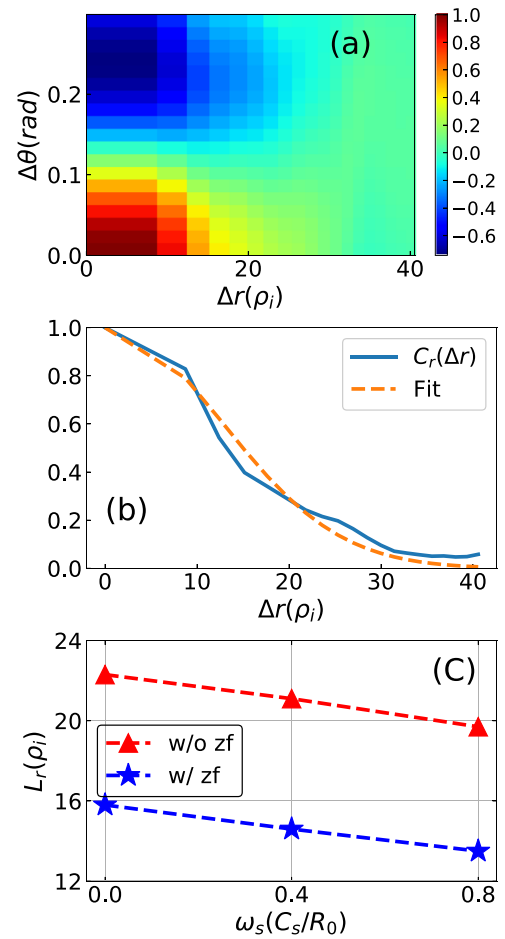

FIG. 8. Panels (a) and (b) show the two dimensions of the correlation function $C_{r\theta}(\Delta r, \Delta\theta)$ and one dimension of the correlation function $C_r(\Delta r)$, respectively, for the case with zonal flow and $\omega_s = 0$. A Gaussian decay is plotted to fit the correlation function in panel (b) to get the correlation length. Panel (c) shows the correlation length of the turbulence L_r as a function of the E_r shear for cases with (blue star) and without (red triangle) zonal flow, respectively.

reduced but persists for longer than in the presence of the zonal flow shown in Figs. 6(e) and 6(f), respectively. In addition, the E_r shear reduces the intensity of $\delta\phi$ turbulence and suppresses its radial spreads as well. In Figs. 6(e) and 6(f) showing the results of the simulation with both the zonal flow and E_r flow shear, the $\delta\phi$ intensity and radial widths of the poloidal $\delta\phi$ turbulence are both reduced, demonstrating that combining the E_r shear and the zonal flow effectively reduces KBM nonlinear saturation amplitude.

Figures 7(a)–7(c) show the time-averaged and volume-averaged particle diffusivity D, ion heat conductivity χ_i, and mean square of the perturbed electrostatic potential $\delta\phi_{rms}^2$ as a function of the E_r shear, respectively. The particle diffusivity is defined as $D = \frac{1}{n\nabla n}\int dv v_r \delta f$, where v_r is the total radial velocity, and the ion heat conductivity is defined as $\chi_i = \frac{1}{n_i \nabla T_i}\int dv\left(\frac{1}{2}m_i v^2 - \frac{3}{2}T\right)v_r f_i$. Here, we used D_{GB} and χ_{GB} for normalization, where $D_{GB} = \chi_{GB} = v_i \rho_i^2/a$, with $v_i = \sqrt{T_i/m_i}$ as the thermal ion speed. Figures 7(a)–7(c) show that all the aforementioned quantities are suppressed by the zonal flow and decrease with increasing E_r shear, indicating that both the zonal flow and the E_r shear can reduce the KBM nonlinear saturation amplitude. Note that the line shape is not symmetric with respect to positive and negative E_r shear due to the background diamagnetic flow shear, which is similar to the result obtained for the linear simulations discussed above. Moreover, the aforementioned quantities change more slowly as the E_r shear changes in the presence of the zonal flow than in

the absence of the zonal flow, which implies that KBM nonlinear saturation amplitude are more sensitive to the E_r shear in the absence of the zonal flow. This result is obtained because the zonal flow decreases the correlation length of the ambient turbulence in the radial direction (see Fig. 6), resulting in a reduction in the effective $E \times B$ shearing rate.

We calculate the two-point correlation function $C_{r\theta}(\Delta r, \Delta\theta) = \frac{\langle\delta\phi(r+\Delta r, \theta+\Delta\theta)\delta\phi(r,\theta)\rangle}{\sqrt{\langle\delta\phi^2(r+\Delta r, \theta+\Delta\theta)\rangle\langle\delta\phi^2(r,\theta)\rangle}}$ to estimate the radial correlation length of the turbulence, where Δr and $\Delta\theta$ represent the radial and poloidal separation, respectively, and $\langle\cdots\rangle$ denotes the average over the poloidal plane at $t = 6.5R_0/C_s$. Figure 8(a) shows the example of $C_{r\theta}(\Delta r, \Delta\theta)$ with the zonal flow at $\omega_s = 0$. Then we use the maximal value along the ridge of $C_{r\theta}(\Delta r, \Delta\theta)$ to obtain the 1D radial correlation function $C_r(\Delta r)$, as shown in Fig. 8(b). Note that although $C_r(\Delta r)$ has a clear tail because of the streamers but still exhibits Gaussian decay for small radial separations, i.e., $C_r(\Delta r) \approx e^{-(\Delta r/L_r)^2}$, where L_r is the radial correlation length, and the dependence of L_r on the shear rate is shown in

Fig. 8(c), for cases with and without zonal flow, respectively. L_r decreases linearly with the increasing of ω_s, which is consistent with the results presented in Refs. 28 and 29. In addition, the zonal flow reduces the radial correlation length of the turbulence significantly because the eigenmode structures are broken into smaller eddies by the zonal flow (see Fig. 6).

V. SUMMARY

In this study, we have performed GTC linear and nonlinear simulations to investigate the effects of a radial electric field on the KBM. Comparing the results of different simulation models with and without kinetic electrons before the addition of E_r shows that kinetic electrons can reduce the KBM growth rate. Then, we demonstrate the consistency of the Doppler shift between simulation and theory with a constant E_r profile. Linear simulations show that the E_r shear reduces the KBM growth rate, i.e., the E_r shear has stabilizing effects on the KBM that becomes stronger with increasing E_r shear. The poloidal contour of $\delta\phi$ shows that the $E \times B$ flow reduces the radial correlation length of the perturbed electrostatic potential and breaks up the eddy structure. In addition, high-n KBM is more sensitive to the E_r shear effects than low-n KBM due to the increase in the effective shearing rate. Nonlinear simulations show that the E_r shear reduces the particle diffusivity and ion heat conductivity, thereby the nonlinear KBM saturation amplitude is decreased. The zonal flow reduces the effects of E_r shear by reducing the effective shearing rate. The poloidal contour of the $\delta\phi$ in the nonlinear phase indicates that the E_r shear suppresses the radial spreads of KBM turbulence and reduces the corresponding radial correlation length. Asymmetrical results are obtained for both linear and nonlinear simulations under positive and negative E_r shear due to the shear of ion diamagnetic flows in plasma. In a future study, we will carry out simulations using a more experimentally realistic E_r profile. We will also consider collision effects and obtain an E_r profile self-consistent with neoclassical transport.[29,52]

AUTHOR DECLARATIONS
Conflict of Interest

The authors have no conflicts to disclose.

Author Contributions

Yichao Chen: Conceptualization (equal); Data curation (equal); Formal analysis (equal); Investigation (equal); Methodology (equal); Software (equal); Validation (equal); Visualization (equal); Writing – original draft (equal); Writing – review & editing (equal). **Yuqing Qin:** Investigation (equal); Methodology (equal); Validation (equal); Writing – review & editing (equal). **Guoya Sun:** Conceptualization (equal); Data curation (equal); Formal analysis (equal); Funding acquisition (equal); Project administration (equal); Resources (equal); Software (equal); Supervision (equal); Validation (equal); Writing – review & editing (equal). **Ge Dong:** Validation (equal); Writing – review & editing (equal). **Yong Xiao:** Methodology (equal); Validation (equal); Visualization (equal). **Zhihong Lin:** Formal analysis (equal); Funding acquisition (equal); Methodology (equal); Project administration (equal); Validation (equal); Visualization (equal); Writing – review & editing (equal).

DATA AVAILABILITY

The data that support the findings of this study are available from the corresponding author upon reasonable request.

REFERENCES

[1]F. Wagner, G. Becker, K. Behringer, D. Campbell, A. Eberhagen, W. Engelhardt, G. Fußmann, O. Gehre, J. Gernhardt, G. Gierke, G. Haas, and M. Huang, Phys. Rev. Lett. **49**, 1408 (1982).
[2]R. Budny, R. Andre, G. Bateman, F. Halpern, C. Kessel, A. Kritz, and D. McCune, Nucl. Fusion **48**, 075005 (2008).
[3]G. De Temmerman, J. Zielinski, S. Diepen, L. Marot, and M. Price, Nucl. Fusion **51**, 073008 (2011).
[4]W. Wan, S. Parker, Y. Chen, Z. Yan, R. Groebner, and P. Snyder, Phys. Rev. Lett. **109**, 185004 (2012).
[5]Y. Zhao, J. Wang, D. Liu, W. Chen, G. Dong, and Z. Lin, Phys. Plasmas **28**, 012107 (2021).
[6]P. Snyder, R. Groebner, A. Leonard, T. Osborne, and H. Wilson, Phys. Plasmas **16**, 056118 (2009).
[7]S. Saarelma, J. Martin-Collar, D. Dickinson, B. F. McMillan, and C. M. Roach, Plasma Phys. Controlled Fusion **59**, 064001 (2017).
[8]Y. Li and Y. Xiao, Phys. Plasmas **24**, 081202 (2017).
[9]H.-s. Xie, Y. Xiao, I. Holod, Z. Lin, and E. Belli, J. Plasma Phys. **82**, 905820503 (2016).
[10]I. Holod, Z. Lin, S. Taimourzadeh, R. Nazikian, D. Spong, and A. Wingen, Nucl. Fusion **57**, 016005 (2016).
[11]D. Hatch, M. Kotschenreuther, S. Mahajan, P. Valanju, F. Jenko, D. Told, T. Görler, and S. Saarelma, Nucl. Fusion **56**, 104003 (2016).
[12]Y. Andrew, N. Hawkes, T. Biewer, K. Crombe, D. Keeling, E. de la Luna, C. Giroud, A. Korotkov, A. Meigs, A. Murari, I. Nunes, R. Sartori, T. Tala, and JET-EFDA Contributors, Europhys. Lett. **83**, 15003 (2008).
[13]J. Schirmer, G. Conway, H. Zohm, W. Suttrop, and ASDEX Upgrade Team, Nucl. Fusion **46**, S780 (2006).
[14]J. Wu, Y. C. Chen, P. Chen, Y. J. Chen, L. M. Yao, and J. L. Fu, IEEE Trans. Plasma Sci. **47**, 457 (2019).
[15]B. Rice, K. Burrell, L. Lao, and Y. Lin-Liu, Phys. Rev. Lett. **79**, 2694 (1997).
[16]J. S. deGrassie, J. A. Boedo, and B. A. Grierson, Phys. Plasmas **22**, 080701 (2015).
[17]X. Xiao, L. Liu, X. F. Zhang, and S. Wang, Phys. Plasmas **18**, 032504 (2011).
[18]K. Burrell, T. Carlstrom, E. Doyle, D. Finkenthal, P. Gohil, R. Groebner, D. Hillis, J. Kim, H. Matsumoto, R. Moyer, T. Osborne, C. Rettig, W. Peebles, T. Rhodes, H. StJohn, R. Stambaugh, M. Wade, and J. Watkins, Plasma Phys. Controlled Fusion **34**, 1859 (2000).
[19]P. W. Terry, Rev. Mod. Phys. **72**, 109 (2000).
[20]C. Ningfei, H. Hu, X. Zhang, S. Wei, and Z. Qiu, Phys. Plasmas **28**, 042505 (2021).
[21]P. Xi, X. Xu, X. Wang, and T. Xia, Phys. Plasmas **19**, 092503 (2012).
[22]W. Wan, S. Parker, Y. Chen, R. Groebner, Z. Yan, A. Pankin, and S. Kruger, Phys. Plasmas **20**, 055902 (2013).
[23]Z. Lin, Y. Nishimura, Y. Xiao, I. Holod, W. Zhang, and L. Chen, Plasma Phys. Controlled Fusion **49**, B163 (2007).
[24]I. Holod, W. Zhang, Y. Xiao, and Z. Lin, Phys. Plasmas **16**, 122307 (2009).
[25]J. Bao and Z. Lin, Phys. Plasmas **24**, 102516 (2017).
[26]K. Fang, J. Bao, and Z. Lin, Plasma Sci. Technol. **21**, 115102 (2019).
[27]S. Taimourzadeh, L. Shi, Z. Lin, R. Nazikian, I. Holod, and D. Spong, Nucl. Fusion **59**, 046005 (2019).
[28]W. Wang, J. Bao, X. Wei, Z. Lin, G. Choi, S. Dettrick, A. Kuley, C. Lau, P. Liu, and T. Tajima, Plasma Phys. Controlled Fusion **63**, 065001 (2021).
[29]J. Fu, J. H. Nicolau, P. Liu, X. Wei, Y. Xiao, and Z. Lin, Phys. Plasmas **28**, 062309 (2021).

[30] W. Lee, J. Comput. Phys. **72**, 243 (1987).

[31] G. Dong, J. Bao, A. Bhattacharjee, A. Brizard, Z. Lin, and P. Porazik, Phys. Plasmas **24**, 081205 (2017).

[32] Z. Lin, W. Tang, and W. Lee, Phys. Plasmas **2**, 2975 (1995).

[33] L. Zheng and M. Tessarotto, Phys. Plasmas **2**, 1250 (1995).

[34] C. Cheng and L. Chen, Nucl. Fusion **21**, 403 (1981).

[35] Y. Chen, S. Parker, G. Rewoldt, S.-H. Ku, G. Park, and C. Chang, Phys. Plasmas **15**, 055905 (2008).

[36] M. Kissick, J. Leboeuf, S. Cowley, J. Dawson, V. Decyk, P.-A. Gourdain, J. Gauvreau, P. Pribyl, L. Schmitz, R. Sydora, and G. Tynan, Phys. Plasmas **6**, 4722 (1999).

[37] J. F. Parisi, F. I. Parra, C. M. Roach, C. Giroud, W. Dorland, D. R. Hatch, M. Barnes, J. C. Hillesheim, N. Aiba, J. Ball, P. G. Ivanov, and JET Contributors, Nucl. Fusion **60**, 126045 (2020).

[38] D. R. Hatch, R. D. Hazeltine, M. K. Kotschenreuther, and S. M. Mahajan, Plasma Phys. Controlled Fusion **60**, 084003 (2018).

[39] A. Ashourvan, R. Nazikian, E. Belli, J. Candy, D. Eldon, B. A. Grierson, W. Guttenfelder, S. R. Haskey, C. Lasnier, G. R. McKee, and C. C. Petty, Phys. Rev. Lett. **123**, 115001 (2019).

[40] T. Hahm and K. Burrell, Phys. Plasmas **2**, 1648 (1995).

[41] P. Abdoul, D. Dickinson, C. Roach, and H. Wilson, Plasma Phys. Controlled Fusion **60**, 025011 (2014).

[42] J. Lang, S. Parker, and Y. Chen, Phys. Plasmas **15**, 055907 (2008).

[43] G. Dong, J. Bao, A. Bhattacharjee, and Z. Lin, Phys. Plasmas **26**, 010701 (2019).

[44] H. Masui, A. Ishizawa, K. Imadera, Y. Kishimoto, and Y. Nakamura, Nucl. Fusion **62**, 074001 (2022).

[45] M. Kotschenreuther, D. Hatch, S. Mahajan, P. Valanju, L. Zheng, and X. Liu, Nucl. Fusion **57**, 064001 (2017).

[46] M. Kotschenreuther, X. Liu, D. Hatch, S. Mahajan, L. Zheng, A. Diallo, R. Groebner, DIII-D Team, J. Hillesheim, C. Maggi, C. Giroud, F. Koechl, V. Parail, S. Saarelma, E. Solano, A. Chankin, and JET Contributors, Nucl. Fusion **59**, 096001 (2019).

[47] G. Ren, J. Li, L. Wei, and Z.-X. Wang, Nucl. Fusion **62**, 096034 (2022).

[48] A. Ishizawa, K. Imadera, Y. Nakamura, and Y. Kishimoto, Phys. Plasmas **26**, 082301 (2019).

[49] S. Maeyama, A. Ishizawa, T.-H. Watanabe, M. Nakata, N. Miyato, M. Yagi, and Y. Idomura, Phys. Plasmas **21**, 052301 (2014).

[50] A. Mishchenko, A. Bottino, T. Hayward-Schneider, E. Poli, X. Wang, R. Kleiber, M. Borchardt, C. Nührenberg, A. Biancalani, A. Könies, E. Lanti, P. Lauber, R. Hatzky, F. Vannini, L. Villard, and F. Widmer, Plasma Phys. Controlled Fusion **64**, 104009 (2022).

[51] H. Y. Wang, I. Holod, Z. Lin, J. Bao, J. Y. Fu, P. F. Liu, J. H. Nicolau, D. Spong, and Y. Xiao, Phys. Plasmas **27**, 082305 (2020).

[52] J. Fu, P. Liu, X. Wei, Z. Lin, N. M. Ferraro, and R. Nazikian, Plasma Sci. Technol. **23**, 105104 (2021).